J. Fluid Mech. (2004), *vol.* 498, *pp.* 123–137.
DOI: 10.1017/S0022112003006608 Printed in the United Kingdom

The drag on needles moving in a Langmuir monolayer

By TH. M. FISCHER

Department of Chemistry and Biochemistry, The Florida State University, Tallahassee, FL 32306, USA
tfischer@chem.fsu.edu

(Received 19 February 2003 and in revised form 1 August 2003)

The motion of membrane-bound objects is important in many aspects of biology and surface chemistry. Here we derive some general relations for objects moving in a surface film overlying a fluid of depth H. A solution to the problem of the drag can be obtained from a two-dimensional system of integral equations. Here we focus on the problem of an ideal needle moving edge-on (in the direction of its tip) or broadside-on (perpendicular to the direction of the tip). It is shown that in comparison to the drag on a circular disk a new scaling regime of the drag on a needle arises when the ratio between surface shear viscosity and subphase viscosity η_s/η is smaller than the length of the needle.

1. Introduction

Rheological measurements of polymeric or amphiphilic monolayers are a subject of current investigation. They play an important role in the dynamic characterization of surfaces in industries ranging from food and pharmaceutical to petroleum. The measurement of surface shear viscosities was pioneered in the last century. The channel flow rheometer was developed by Harkins & Myers (1937), Jarvis (1965), and Mannheimer & Schechter (1970) and revived recently by Schwartz, Knobler & Bruinsma (1994). Cylindrical rheometers have the advantage of using symmetry arguments to simplify the hydrodynamic equations and therefore the mathematical analysis. Consequently there is a rich variety of different cylindrical symmetric rheometers (Langmuir & Schaefer 1937; Fourt & Harkins 1938; Goodrich & Chatterjee 1970; Lifshutz, Hedge & Slattery 1971; Goodrich, Allen & Poskanzer 1975; Oh & Slattery 1978; Klingler & McConnell 1993; Ghaskadvi *et al.* 1997; Barentin *et al.* 1999; Steffen *et al.* 2001; Wurlitzer, Schmiedel & Fischer 2002) the mathematics of which has been outlined by Saffmann & Delbrück (1975), Hughes, Pailthorpe & White (1981) and Stone & Ajdari (1998).

Recently interest has moved back toward non-symmetric needle-shaped rheometers (Brooks *et al.* 1999; Ding *et al.* (2002*b*), Ding, Warriner & Zasadzinski 2002*a*) through claims that needle-shaped objects should have some advantages because of their sensitivity to the surface shear viscosity compared to the subphase rheological background force. The needle viscometer, compared to the rotating knife edge and other rheometers of cylindrical symmetry, has a lower ratio between the area of the needle facing the subphase and the perimeter of the monolayer/needle boundary. Therefore the sensitivity of a needle viscometer for the measurement of surface shear viscosity should be better than that of a disk viscometer of comparable size.

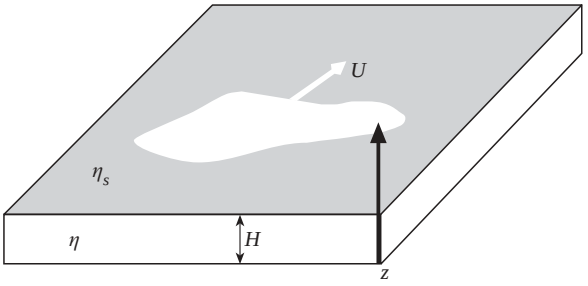

FIGURE 1. Sketch of a solid two-dimensional object immersed in a surface of viscosity η_s on a subphase of depth H and viscosity η.

Here we derive the drag force on an ideal needle of vanishing thickness and we provide the mathematical description using an approach similar to Levine, Liverpool & MacKintosh (2003), which differs from the work of Shahin (1986). We show that the sensitivity of a disk and a needle viscometer is exactly the same in the high-surface-viscosity regime if the length of the needle is 3.3 (10.9) times the diameter of a comparable disk viscometer when the needle moves in deep (shallow) water. The needle viscometer is indeed more sensitive to the surface shear viscosities than comparably sized disk viscometers if the value of the ratio between the surface and bulk viscosity lies between the width and the length of the needle. However in this regime, in contrast to assumptions made in Brooks *et al.* (1999) and Ding *et al.* (2002*a*, *b*), the relation between drag force and flow velocity is nonlinear in the Boussinesq number. In the regime where the viscosity ratio is smaller than the width of the needle sensitivity to the surface viscosity is lost. As a consequence, surface shear viscosity data acquired with the needle viscometer at low Boussinesq numbers needs to be reanalysed.

2. Hydrodynamic drag on objects of arbitrary shape

Consider a solid two-dimensional object moving in a monolayer of surface shear viscosity η_s (the surface pressure and surface viscosity have the dimensions of their three-dimensional analogues muliplied by a length) on top of a laterally infinitely extended subphase of viscosity η and depth H (figure 1). The flow of the subphase is described by Stokes' equation and the continuity equation:

$$\left.\begin{aligned} -\nabla p + \eta \boldsymbol{\Delta}\, \boldsymbol{u} = \boldsymbol{0}, \\ \nabla \cdot \boldsymbol{u} = 0, \end{aligned}\right\} \tag{2.1}$$

where p is the subphase pressure and $\boldsymbol{u}$ denotes the subphase velocity which vanishes at the bottom ($z = 0$) of the subphase layer. The dynamic stress tensor is given by

$$\boldsymbol{\sigma} = -p\mathbf{1} + \eta(\nabla \boldsymbol{u} + [\nabla \boldsymbol{u}]^t) \tag{2.2}$$

where $\mathbf{1}$ denotes the unit tensor in three-dimensional space. The air/water surface is assumed to be flat and located at the position $z = H$. At this surface boundary conditions have to be fulfilled. Within the area of the surface A covered by the two-dimensional object the surface velocity $\boldsymbol{u}_s = \boldsymbol{u}(z = H)$ must coincide with the

velocity $U\boldsymbol{e}_x$ of the object:

$$\boldsymbol{u}_s = U\boldsymbol{e}_x \quad \text{for} \quad \boldsymbol{r}_s \in A \tag{2.3}$$

while at the monolayer-covered surface the flow can be approximated by an incompressible 2d-Stokes flow:

$$\left.\begin{aligned} -\nabla_s\pi_s + \eta_s\boldsymbol{\Delta}_s\boldsymbol{u}_s + \eta\frac{\partial\boldsymbol{u}}{\partial z}\bigg|_s &= \boldsymbol{0} \\ \nabla_s\cdot\boldsymbol{u}_s &= 0 \end{aligned}\right\} \quad \text{for} \quad \boldsymbol{r}_s \notin A, \tag{2.4}$$

where π_s is the surface pressure, $\boldsymbol{u}_s$ the surface velocity and ∇_s denotes the surface gradient. The surface dynamic stress tensor is given by

$$\boldsymbol{\sigma}_s = -\pi_s\boldsymbol{\delta} + \eta_s(\nabla_s\boldsymbol{u}_s + [\nabla_s\boldsymbol{u}_s]^t) \tag{2.5}$$

where $\boldsymbol{\delta} = \mathbf{1} - \boldsymbol{e}_z\boldsymbol{e}_z$ is the surface idem factor. The general solution of (2.1) can be written as

$$\left.\begin{aligned} \boldsymbol{u} &= \nabla\Xi + \nabla\times(\boldsymbol{e}_z\Psi) + \boldsymbol{r}_s\cdot\nabla_s\nabla\Pi + \boldsymbol{e}_z\frac{\partial\Pi}{\partial z}, \\ p &= -\eta\frac{\partial^2\Pi}{\partial z^2}, \end{aligned}\right\} \tag{2.6}$$

where $\boldsymbol{r}_s = \boldsymbol{\delta}\cdot\boldsymbol{r}$ is the projection of the vector $\boldsymbol{r}$ onto the monolayer plane, and Ξ, Ψ and Π are scalar functions solving the Laplace equation (Happel & Brenner 1983). From the velocity boundary conditions $u_z(z = H) = 0$ and from the incompressibility of the monolayer phase it follows that $\Pi = \Xi = 0$ and all streamlines are lying in planes parallel to the air/water interface (Stone & Ajdari 1998). The drag force on the object arises from a subphase and a monolayer component:

$$\left.\begin{aligned} \boldsymbol{F}_{drag} &= \boldsymbol{F}_{sub} + \boldsymbol{F}_{mon}, \\ \boldsymbol{F}_{sub} &= \int_A \boldsymbol{\sigma}\cdot\boldsymbol{e}_z\,\mathrm{d}^2\boldsymbol{r}_s, \\ \boldsymbol{F}_{mon} &= \oint_{\partial A}\boldsymbol{\sigma}_s\cdot\boldsymbol{n}\,\mathrm{d}s. \end{aligned}\right\} \tag{2.7}$$

One way of solving the set of equations (2.1), (2.3), (2.4) is to replace the boundary condition (2.3) by the equation.

$$\left.\begin{aligned} \boldsymbol{f} - \nabla_s\pi_s + \eta_s\boldsymbol{\Delta}_s\boldsymbol{u}_s + \eta\frac{\partial\boldsymbol{u}}{\partial z}\bigg|_s &= \boldsymbol{0} \\ \nabla_s\cdot\boldsymbol{u}_s &= 0 \end{aligned}\right\} \quad \text{for} \quad \boldsymbol{r}_s \in A, \tag{2.8}$$

where $\boldsymbol{f}$ is a surface force density, to be chosen such that (2.3) is satisfied. The velocity field $\boldsymbol{u}$ fulfils the Laplace equation and hence can be written as

$$\boldsymbol{u}(\boldsymbol{r}_s + z\boldsymbol{e}_z) = \int \mathrm{d}^2\boldsymbol{k}\,\mathrm{e}^{\mathrm{i}\boldsymbol{k}\cdot\boldsymbol{r}_s}\frac{\sinh kz}{\sinh kH}\hat{\boldsymbol{u}}_s(\boldsymbol{k}). \tag{2.9}$$

Fourier transformation converts (2.4) and (2.8) into a two-dimensional algebraic matrix equation. The Fourier transform of (2.8*b*) is $\boldsymbol{k}\cdot\hat{\boldsymbol{u}} = 0$. Multiplication of $\boldsymbol{\delta} - \boldsymbol{k}\boldsymbol{k}/k^2$ by the Fourier transform of (2.8*a*) then leads to this algebraic equation for

the velocity $\hat{\boldsymbol{u}}_s$:

$$\left.\begin{aligned}\hat{\boldsymbol{u}}_s(\boldsymbol{k}) &= \hat{\boldsymbol{O}}(\boldsymbol{k})\cdot\hat{\boldsymbol{f}}(\boldsymbol{k}),\\ \hat{\boldsymbol{O}}(\boldsymbol{k}) &= \frac{k^2\boldsymbol{\delta}-\boldsymbol{k}\,\boldsymbol{k}}{\eta k^3(\coth kH+\mathscr{B}ka)},\end{aligned}\right\} \tag{2.10}$$

where $\hat{\boldsymbol{O}}(\boldsymbol{k})$ is the surface Oseen tensor, a is a typical length scale of the object and

$$\mathscr{B} = \frac{\eta_s}{\eta a} \tag{2.11}$$

is the Boussinesq number. The boundary conditions (2.4) and (2.8) are diffuse in Fourier space and it is useful to perform an inverse Fourier transformation which leads to

$$\boldsymbol{u}_s(\boldsymbol{r}_s) = \int_A \mathrm{d}^2\boldsymbol{r}'_s\,\boldsymbol{O}(\boldsymbol{r}_s-\boldsymbol{r}'_s)\cdot\boldsymbol{f}(\boldsymbol{r}'_s) \tag{2.12}$$

with $\boldsymbol{O}(\boldsymbol{r}_s)$ the Oseen tensor in real space. The inverse Fourier transformation can be performed analytically in the deep water limit $H\to\infty$ and shallow water limit $H\to 0$. One finds (Appendix A)

$$\begin{aligned}\boldsymbol{O}(\boldsymbol{r}_\mathrm{s}, H\to\infty) = {}& \frac{2\boldsymbol{r}_\mathrm{s}\boldsymbol{r}_\mathrm{s}-\boldsymbol{\delta}r_s^2}{r_s^2}\frac{1}{4\eta r_s}\left\{\mathrm{H}_1\left(\frac{r_s}{\mathscr{B}a}\right)-N_1\left(\frac{r_s}{\mathscr{B}a}\right)-\frac{2\mathscr{B}a}{\pi r_s}\right\}\\ &+\frac{r_s^2\boldsymbol{\delta}-\boldsymbol{r}_\mathrm{s}\boldsymbol{r}_\mathrm{s}}{r_s^2}\frac{1}{4\eta\mathscr{B}a}\left\{\mathrm{H}_0\left(\frac{r_s}{\mathscr{B}a}\right)-N_0\left(\frac{r_s}{\mathscr{B}a}\right)\right\},\end{aligned} \tag{2.13a}$$

$$\begin{aligned}\boldsymbol{O}(\boldsymbol{r}_\mathrm{s}, H\to 0) = {}& \frac{2\boldsymbol{r}_\mathrm{s}\boldsymbol{r}_\mathrm{s}-\boldsymbol{\delta}r_s^2}{r_s^2}\frac{H}{2\pi\eta r_s^2}\left[1-\frac{r_s}{\sqrt{\mathscr{B}Ha}}K_1\left(\frac{r_s}{\sqrt{\mathscr{B}Ha}}\right)\right]\\ &+\frac{\boldsymbol{\delta}r_s^2-\boldsymbol{r}_\mathrm{s}\boldsymbol{r}_\mathrm{s}}{r_s^2}\frac{1}{2\pi\eta\mathscr{B}a}K_0\left(\frac{r_s}{\sqrt{\mathscr{B}Ha}}\right),\end{aligned} \tag{2.13b}$$

where H_n, N_n, and K_n are Struve functions, Bessel functions and modified Bessel functions of the second kind of order n (Gradshteyn & Ryshik 1981, 8.550, 8.403 and 8.446). Oseen's tensor satisfies the following asymptotic behaviour:

$$\boldsymbol{O}(\boldsymbol{r}_\mathrm{s}/\mathscr{B}a\to 0, H\to\infty)\approx\frac{1}{4\eta\pi\mathscr{B}a}\frac{\boldsymbol{r}_\mathrm{s}\boldsymbol{r}_\mathrm{s}}{r_s^2}+\frac{\ln(2\mathscr{B}a/r_s)-\gamma-1/2}{4\eta\pi\mathscr{B}a}\boldsymbol{\delta}, \tag{2.14a}$$

$$\boldsymbol{O}(\boldsymbol{r}_\mathrm{s}/\mathscr{B}a\to\infty, H\to\infty)\approx\frac{1}{2\pi\eta r_s}\frac{\boldsymbol{r}_\mathrm{s}\boldsymbol{r}_\mathrm{s}}{r_s^2}-\frac{\mathscr{B}a}{2\pi\eta r_s^2}\frac{2\boldsymbol{r}_\mathrm{s}\boldsymbol{r}_\mathrm{s}-\boldsymbol{\delta}r_s^2}{r_s^2}, \tag{2.14b}$$

$$\boldsymbol{O}(\boldsymbol{r}_\mathrm{s}/\mathscr{B}a\to 0, H\to 0)\approx\frac{1}{4\eta\pi\mathscr{B}a}\frac{\boldsymbol{r}_\mathrm{s}\boldsymbol{r}_\mathrm{s}}{r_s^2}+\frac{\ln\sqrt{4\mathscr{B}aH/r_s^2}-\gamma-1/2}{4\eta\pi\mathscr{B}a}\boldsymbol{\delta}, \tag{2.14c}$$

$$\begin{aligned}\boldsymbol{O}(\boldsymbol{r}_\mathrm{s}/\mathscr{B}a\to\infty, H\to 0)\approx{}& \frac{H}{2\pi\eta r_s^2}\frac{\boldsymbol{r}_\mathrm{s}\boldsymbol{r}_\mathrm{s}-\boldsymbol{\delta}r_s^2}{r_s^2}\\ &-\frac{H^{1/4}}{2^{3/2}\pi^{1/2}\eta(\mathscr{B}a)^{3/4}r_s^{1/2}}\exp(-r_s/\sqrt{\mathscr{B}aH})\frac{2\boldsymbol{\delta}r_s^2-\boldsymbol{r}_\mathrm{s}\boldsymbol{r}_\mathrm{s}}{r_s^2},\end{aligned} \tag{2.14d}$$

where $\gamma=0.577216$ denotes Euler's constant. Equations (2.3) and (2.12) define a two-dimensional integral equation for the force density $\boldsymbol{f}$. The drag force on the object in terms of the force density $\boldsymbol{f}$ is given by

$$\boldsymbol{F}_{drag} = \int_A \mathrm{d}^2\boldsymbol{r}_\mathrm{s}\;\boldsymbol{f}(\boldsymbol{r}_\mathrm{s}). \tag{2.15}$$

3. The drag force on an ideal needle

3.1. (*Edge-on*) *motion*

If the object is a thin needle of length $2a$ and width $2b$ where $b \ll a$ and $b \ll \mathscr{B}a$ moving in the direction of its tip (edge-on), then the needle velocity, the force density and all vectors connecting different positions on the needle point along the needle. For this reason the problem reduces to a one-dimensional integral equation, where the width b drops out of the equation. Choosing the x-direction as the direction of the needle this equation is

$$\frac{\eta U a}{F^{\parallel}_{drag}}(H \to \infty) = \frac{\displaystyle\int_{-a}^{a} \mathrm{d}x' \, \frac{a}{4|x-x'|}\left[\mathrm{H}_1\left(\frac{|x-x'|}{\mathscr{B}a}\right) - N_1\left(\frac{|x-x'|}{\mathscr{B}a}\right) - \frac{2\mathscr{B}a}{\pi|x-x'|}\right]\tau_x(x')}{\displaystyle\int_{-a}^{a} \mathrm{d}x' \, \tau_x(x')} \quad \text{for all } -a < x < a, \tag{3.1a}$$

$$\frac{\eta U a}{F^{\parallel}_{drag}}(H \to 0) = \frac{\displaystyle\int_{-a}^{a} \mathrm{d}x' \, \frac{Ha}{2\pi|x-x'|^2}\left[1 - \frac{|x-x'|}{\sqrt{\mathscr{B}Ha}} K_1\left(\frac{|x-x'|}{\sqrt{\mathscr{B}Ha}}\right)\right]\tau_x(x')}{\displaystyle\int_{-a}^{a} \mathrm{d}x' \, \tau_x(x')} \quad \text{for all } -a < x < a, \tag{3.1b}$$

where $\tau_x = 2bf_x$ is the x-component of a one-dimensional force density. For large Boussinesq number $\mathscr{B} \to \infty$ the asymptotic expression of the Oseen tensor for $\boldsymbol{r}_s/\mathscr{B}a \to \boldsymbol{0}$ can be used, and the solution to (3.1) is

$$\tau_x(x) = \frac{F^{\parallel}_{drag}}{\pi\sqrt{a^2 - x^2}} \quad \text{for} \quad \mathscr{B} \to \infty \tag{3.2}$$

which leads to

$$F^{\parallel}_{drag} = \begin{cases} 4\pi\eta a U \dfrac{\mathscr{B}}{\ln(4\mathscr{B}) - \gamma + 1/2} & \text{for} \quad \mathscr{B} \to \infty, H \to \infty \qquad (3.3a) \\[2ex] \dfrac{4\pi\eta a^2 U}{H} \dfrac{\mathscr{B}H/a}{\ln(4\sqrt{\mathscr{B}H/a}) - \gamma + 1/2} & \text{for} \quad \mathscr{B} \to \infty, H \to 0. \qquad (3.3b) \end{cases}$$

This should be compared with the drag on a circular disk which is (Saffmann & Delbrück 1975; Hughes *et al.* 1981; Barentin *et al.* 1999):

$$F^{disk}_{drag} = \begin{cases} 4\pi\eta a U \dfrac{\mathscr{B}}{\ln(2\mathscr{B}) - \gamma} & \text{for} \quad \mathscr{B} \to \infty, H \to \infty, \qquad (3.4a) \\[2ex] \dfrac{4\pi\eta a^2 U}{H} \dfrac{\mathscr{B}H/a}{\ln(2\sqrt{\mathscr{B}H/a}) - \gamma} & \text{for} \quad \mathscr{B} \to \infty, H \to 0. \qquad (3.4b) \end{cases}$$

Hence for large Boussinesq numbers at similar viscosities and water depths, the drag on a needle equals that on a disk if its length is $2\sqrt{\mathrm{e}} = 3.3$ ($H \gg a$) or $4\mathrm{e} = 10.9$ ($H \ll a$) times longer than the diameter of the disk. For $\mathscr{B} \to 0$ the Oseen tensor transmits a shorter-range hydrodynamic interaction such that the force profile $\tau_x(x)$ flattens with less pronounced singularities at the edges of the needle. A constant force

profile

$$\tau_x(x) = \frac{F^{\parallel}_{drag}}{2a} \quad \text{for} \quad \mathscr{B} \to 0 \tag{3.5}$$

becomes a very good approximation except close to the edges. Averaging the velocity profile across the needle with this force profile gives (Appendix B)

$$F^{\parallel}_{drag} \approx \begin{cases} \dfrac{2\pi\eta a U}{\ln(0.96/\mathscr{B})} & \text{for} \quad \mathscr{B} \to 0,\ H \to \infty, \qquad (3.6a) \\ \dfrac{4\eta a^2 U}{H}\sqrt{\mathscr{B}H/a}\left(1 + \dfrac{\ln(1/\sqrt{\mathscr{B}H/a}) + \gamma + 1}{\pi}\sqrt{\mathscr{B}H/a}\right) & \\ \qquad\qquad \text{for} \quad \mathscr{B} \to 0,\ H \to 0. \qquad (3.6b) \end{cases}$$

Equation (2.5) holds in frequency space, i.e. $\boldsymbol{\sigma}_s = \boldsymbol{\sigma}_s(\omega)$, $\pi_s = \pi_s(\omega)$ and $\eta_s = \eta_s(\omega)$ such that time-dependent oscillatory movements of the needle may also be described. In this case surface viscoelastic effects might render the viscosity and hence the Boussinesq number $\mathscr{B}$ complex. Both $F^{\parallel}_{drag}/U$ and $\mathscr{B}$ will have a phase and an amplitude. No *a priori* knowledge of the frequency dependence of the viscosity $\eta_s(\omega)$ is required since in the linear response regime and in the absence of inertial effects the Stokes equation for different frequency decouples.

For Boussinesq numbers of order $\mathscr{B} \approx 1$ the force profile $\tau_x(x)$ lies between equation (3.2) and equation (3.5) and one needs to solve equation (3.1*a*) numerically. Discretizing equation (3.1) turns the integral equation into a matrix inversion problem, which may be solved by standard techniques (Appendix C). In Figure 2 we double logarithmically plot the amplitude of the drag force on a needle in deep water versus the Boussinesq number amplitude $|\mathscr{B}|$. As can be seen both, asymptotics fit the data well in the regions $|\mathscr{B}| < 0.1$ and $|\mathscr{B}| > 2$. In the region which is not fitted well by the asymptotics the data are also displayed on a linear scale. In the entire range the force amplitude is almost independent of the Boussinesq number phase arg ($\mathscr{B}$) and surface viscous or surface elastic effects lead to the same force amplitudes. The distinction between viscous and elastic effects can be determined from the drag force phase $\arg(F^{\parallel}_{drag}/U)$. The Boussinesq number phase $\arg(\mathscr{B})$ is proportional to the drag force phase $\arg(F^{\parallel}_{drag}/U)$ with a factor depending on the Boussinesq number amplitude $|\mathscr{B}|$. For large Boussinesq number amplitudes both phases $\arg(F^{\parallel}_{drag}/U)$ and $\arg(\mathscr{B})$ are the same, while for smaller Boussinesq number amplitudes the phaselag between force and velocity vanishes logarithmically.

Figure 3 shows the drag on the needle on a shallow subphase. The asymptotic curves fit the data in the regions $|\mathscr{B}H/a| < 10^{-3}$ and $|\mathscr{B}H/a| > 1$. The cross-over region is plotted linearly in the inset. The phase between force and velocity changes from half the phase of the Boussinesq number toward the full phase $\arg(\mathscr{B})/2 < \arg(F/U) < \arg(\mathscr{B})$. As can be seen from both figures a linear fit in the Boussinesq number as applied by Brooks *et al.* (1999) and Ding *et al.* (2002*a*, *b*) contradicts both these findings.

3.2. *Broadside-on motion*

The x-, and y-components of the drag force and velocity are decoupled also for a broadside-on motion (i.e. perpendicular to the direction of the tip). Let us choose the x-coordinate as the direction of the motion and the y-direction as the direction of

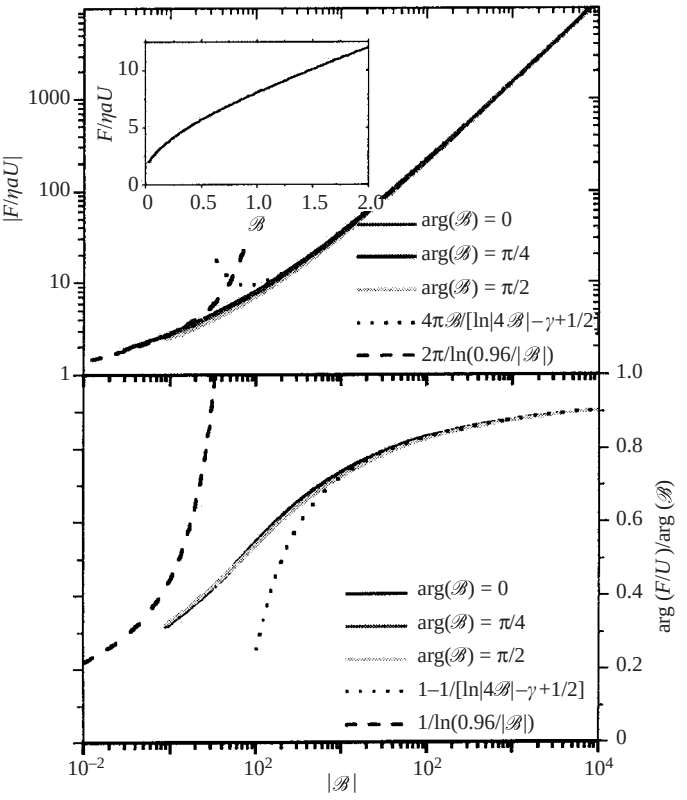

FIGURE 2. Amplitude and phase ratio of the drag force upon a needle of length $2a$ moving edge-on in an incompressible surface of viscosity η_s upon a subphase of viscosity η and infinite depth, plotted double logarithmically as a function of the Boussinesq number amplitude $|\mathscr{B}|$ for three different phases $\arg(\mathscr{B})$. Dotted and dashed lines are asymptotics according to (3.3) and (3.6). The cross-over region where none of the asymptotics describes the numerical data is depicted in a linear plot in the inset of the figure.

the needle. The integral equation for the force density is then

$$\frac{\eta U a}{F^{\perp}_{drag}}(H \to \infty) = \frac{\displaystyle\int_{-a}^{a} \mathrm{d}y' \, \frac{a}{4}\frac{\partial}{\partial y}\left[\mathrm{H}_1\left(\frac{|y-y'|}{\mathscr{B}a}\right) - N_1\left(\frac{|y-y'|}{\mathscr{B}a}\right) - \frac{2\mathscr{B}a}{\pi|y-y'|}\right]\tau_x(y')}{\displaystyle\int_{-a}^{a} \mathrm{d}y' \, \tau_x(y')}$$

$$\text{for all } -a < y < a, \quad (3.7a)$$

$$\frac{\eta U a}{F^{\perp}_{drag}}(H \to 0) = \frac{\displaystyle\int_{-a}^{a} \mathrm{d}y' \, \frac{\partial}{\partial y}\frac{Ha}{2\pi(y-y')}\left[1 - \frac{|y-y'|}{\sqrt{\mathscr{B}Ha}}K_1\left(\frac{|y-y'|}{\sqrt{\mathscr{B}Ha}}\right)\right]\tau_x(y')}{\displaystyle\int_{-a}^{a} \mathrm{d}y' \, \tau_x(y')}$$

$$\text{for all } -a < y < a, \quad (3.7b)$$

and at large Boussinesq numbers we find the same asymptotic equation (3.2) for the force profile on the needle with the argument x replaced by y. At small Boussinesq number (3.5) remains valid for the deep water limit, while for the shallow water limit

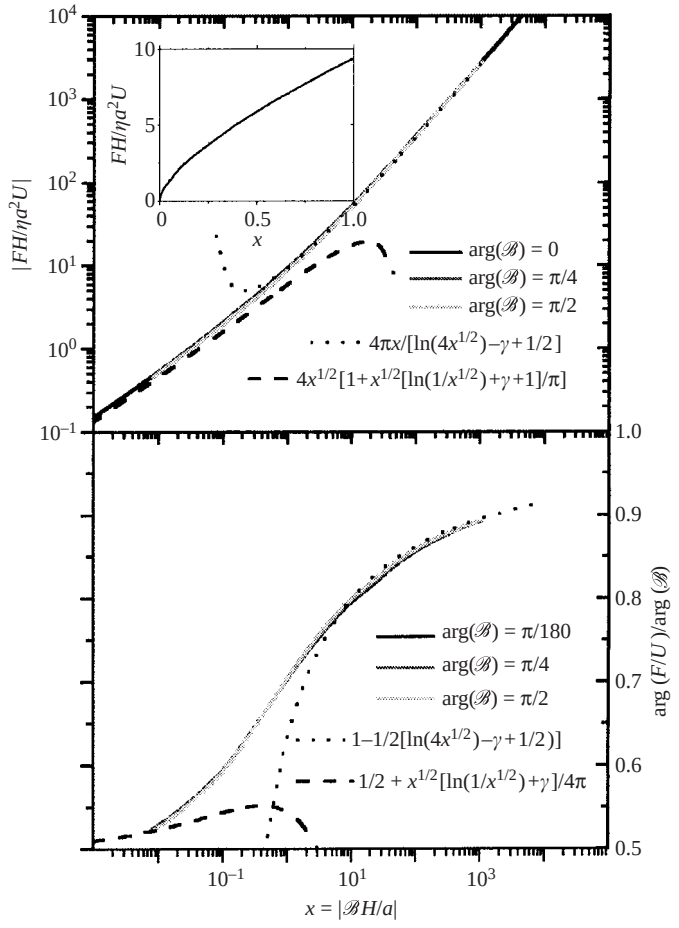

FIGURE 3. As figure 2 but for a subphase of depth $H \ll a$.

we find

$$\tau_x(y) \approx \frac{2F^{\perp}_{drag}}{\pi a^2}\sqrt{a^2-y^2} \quad \text{for} \quad \mathscr{B} \to 0,\ H \to 0. \tag{3.8}$$

The asymptotic drag forces found from this are

$$F^{\perp}_{drag} = \begin{cases} 4\pi\eta a U \dfrac{\mathscr{B}}{\ln(4\mathscr{B}) - \gamma - 1/2} & \text{for} \quad \mathscr{B} \to \infty,\ H \to \infty \\ \dfrac{4\pi\eta a^2 U}{H} \dfrac{\mathscr{B}H/a}{\ln(4\sqrt{\mathscr{B}H/a}) - \gamma - 1/2} & \text{for} \quad \mathscr{B} \to \infty,\ H \to 0 \end{cases} \tag{3.9}$$

and

$$F^{\perp}_{drag} \approx \frac{2\pi\eta a U}{1 - \frac{1}{2}\mathscr{B}\,(\ln(1/\mathscr{B}) + \gamma)} \quad \text{for} \quad \mathscr{B} \to 0,\ H \to \infty. \tag{3.10}$$

At high surface shear viscosities a broadside moving needle experiences the same drag as an edge-on moving needle if it is shorter by the factor 1/e than the edge-on moving needle. In Figure 4 we double logarithmically plot the amplitude of the broadside drag force on a needle in deep water versus the Boussinesq number amplitude $|\mathscr{B}|$ for $\arg(\mathscr{B}) = \pi/180, \pi/4$ and $\pi/2$. Similarly to the edge-on movement, the amplitude

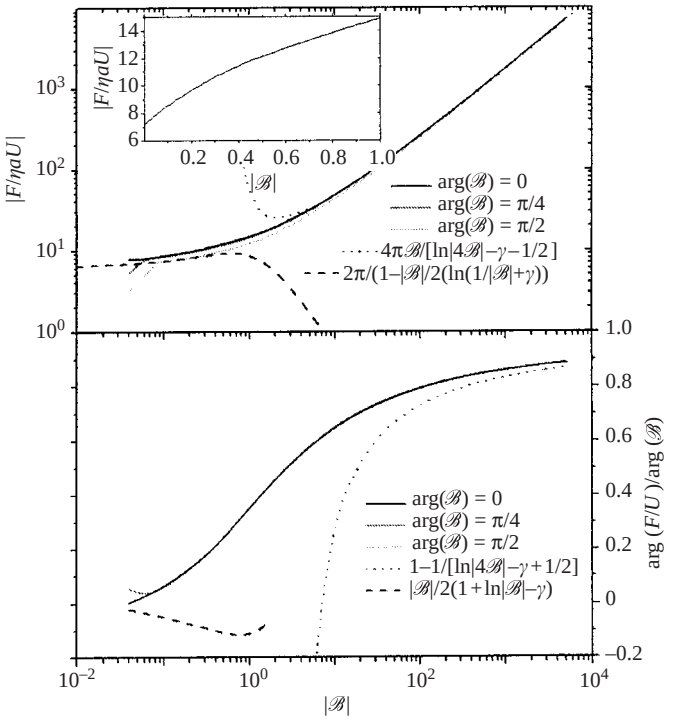

FIGURE 4. Amplitude and phase ratio of the drag force upon a needle of length $2a$ moving broadside-on in an incompressible surface of viscosity η_s upon a subphase of viscosity η and infinite depth, plotted double logarithmically as a function of the Boussinesq number amplitude $\mathscr{B}$ for three different phases $\arg(\mathscr{B})$. Dotted and dashed lines are asymptotics according to (3.9) and (3.10). The cross-over region where none of the asymptotics describes the numerical data, is depicted in a linear plot in the inset of the figure.

of the drag force is not sensitive to the phase of the Boussinesq number. In contrast to the edge-on drag, the drag starts at a finite value for $\mathscr{B} = 0$ and then increases. The phase between the drag and the velocity is proportional to the phase of the Boussinesq number $\arg(F/U) \propto \arg(\mathscr{B})$ at large $\mathscr{B}$.

Figure 5 shows the broadside drag on the needle on a shallow subphase. At large Boussinesq numbers the drag amplitude increases with the amplitude of the Boussinesq number independent of the phase. At small Boussinesq number the drag also depends on the phase of the Boussinesq number.

4. Discussion

The drag force calculated here is that of an ideal (infinitely thin) needle immersed in a monolayer of infinite extent. Real needles used in experiments have a finite width and depth and lateral extent are finite. However, when $\mathscr{B}a$ is small compared to the lateral extent of the monolayer, and large compared to the width and depth of the needle the behaviour displayed in figures 2–5 should still hold. If one reduces the surface viscosity such that $\mathscr{B}a \approx b$ the drag force will depart from the ideal curve and cross-over toward a constant drag determined entirely by the water viscosity (Levine *et al.* 2003).

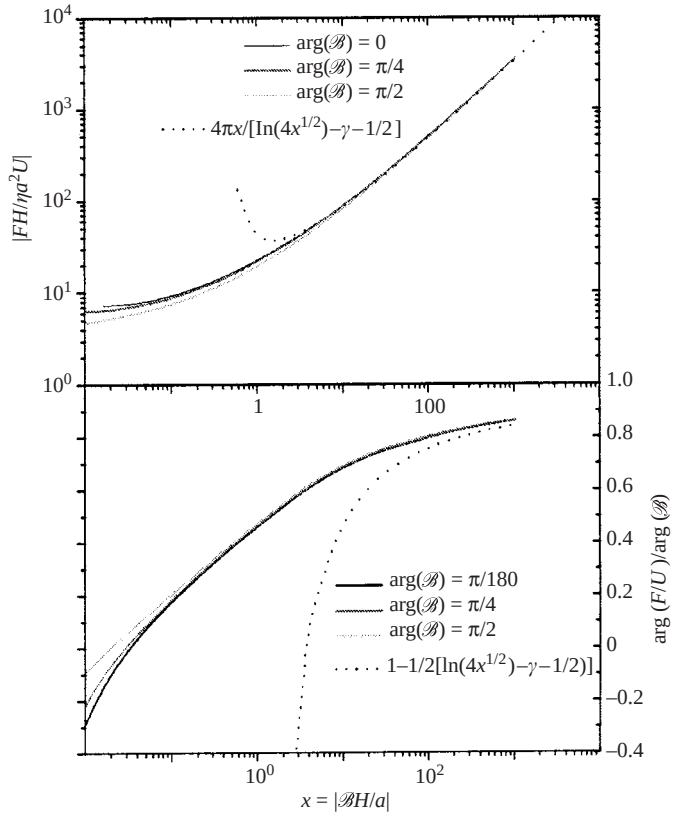

FIGURE 5. As figure 4 but for a subphase of depth $H \ll a$. Dotted lines are asymptotics according to (3.9).

In experiments with the needle viscometer (Brooks *et al.* 1999; Ding *et al.* 2002*a*, *b*) a linear relation between drag and Boussinesq number was used. This gives good results if one works in the regime $\mathscr{B}a \gg 1$ (Brooks *et al.* 1999), where the constant term can be neglected and the logarithmic correction is weak. However as one enters the regime $b/a < \mathscr{B} < 1$ the linear approximation is inadequate and leads to erroneous results (Ding *et al.* 2002*a*, *b*).† The real advantage of working with a needle as compared to a disk arises from the fact that the needle is still sensitive to the surface viscosity in the regime $b/a < \mathscr{B} < 1$ where the disk drag no longer changes with $\mathscr{B}$. The drawback of using a needle is loss of symmetry, leading to more complicated relations between drag and surface viscosity in the regime $b/a < \mathscr{B} < 1$, where this loss of symmetry becomes apparent in the flow profile. Here we have given the precise relationships for needles longer than the depth of the water and for needles in deep water. A disk of the diameter of the width of a needle is more sensitive to the surface viscosity

† For example Ding *et al.* (2002*b*) estimate the surface shear viscosity of DPPC in the liquid condensed/liquid expanded coexistence region using a magnetic needle viscometer to be in the range of 1 msP$< \eta_s <$1 sP (1 sP = 1 surface Poise = 1 g s^{-1}), in contradiction to Klingler McConnell's (1993) measurements ($\eta_s < \mu$ sP) using Browninan motion. Schwartz *et al.* (1994) found the surface shear viscosity of the same coexistence region in pentadecanoic acid to be below $\eta_s < 10^{-5}$ sP using a channel flow viscometer. Using a linear relation between the force and the viscosity obviously leads to surface shear viscosities that are overestimated by orders of magnitude.

than is the needle, which in turn is more sensitive to the surface viscosity than a disk of a diameter comparable to the length of the needle. If one miniaturizes the object experiencing the viscous drag, it makes more sense to perform the miniaturization in both lateral directions rather than in one.

The drag on objects in the monolayer is non-analytic in the limit of large surface viscosity and always reduced by the subphase viscosity as compared to the isolated monolayer system. Translational motion of objects therefore is less sensitive to the surface shear viscosity than rotational motion, which has an analytical behaviour in the limit of large surface viscosities.† A surface rheometer of highest sensitivity hence will be a rheometer making use of miniaturized circular rotating disks immersed in the surface.

5. Conclusions

The drag on a needle in deep and shallow water has been calculated numerically. Asymptotic expressions for small and large Boussinesq numbers have been derived. A linear relation between the drag force and the surface shear viscosity as used by Brooks *et al.* (1999) and Ding *et al.* (2002*a*, *b*) fails to describe the behaviour in the regime where the ratio between surface viscosity and bulk viscosity is smaller than the length of the needle. Data extracted from experiments with needle viscometers need to be reanalysed.

I thank H. Stone for proposing the calculation of the broadside-on motion and for many useful comments, H. Möhwald for generous support, D. K. Schwartz, Grigor Bantchev and P. Heinig for stimulating discussions.

Appendix A. Oseen tensor in direct space

The Oseen tensor in direct space is

$$\boldsymbol{O}(\boldsymbol{r}_s) = \frac{1}{(2\pi)^2} \int \mathrm{d}^2\boldsymbol{k}\hat{\boldsymbol{O}}(\boldsymbol{k})\mathrm{e}^{-\mathrm{i}\boldsymbol{k}\cdot\boldsymbol{r}_s}. \tag{A 1}$$

A.1. *Deep water limit*

Here we derive the Oseen tensor $\boldsymbol{O}(\boldsymbol{r}_s)$ in real space in the limit $H \to \infty$. We decompose the two-dimensional vector $\boldsymbol{k}$ and the Oseen tensor into its components $k\cos\theta$ and $k\sin\theta$ along and perpendicular to $\boldsymbol{r}_s$ to obtain

$$\begin{aligned}
\boldsymbol{O}(\boldsymbol{r}_s) &= \frac{1}{(2\pi)^2}\int_{-\pi}^{\pi}\mathrm{d}\theta\int_0^\infty k\,\mathrm{d}k \begin{pmatrix} \sin^2\theta & -\sin\theta\cos\theta \\ -\sin\theta\cos\theta & \cos^2\theta \end{pmatrix} \frac{\mathrm{e}^{-\mathrm{i}kr_s\cos\theta}}{\eta k(1+\mathscr{B}ka)} \\
&= \frac{1}{(2\pi)^2}\int_0^\infty \mathrm{d}k \begin{pmatrix} \dfrac{2\pi J_1(kr_s)}{kr_s} & 0 \\ 0 & 2\pi\left(J_0(kr_s) - \dfrac{J_1(kr_s)}{kr_s}\right) \end{pmatrix} \frac{1}{\eta(1+\mathscr{B}ka)} \\
&= \frac{1}{(2\pi)}\int_0^\infty \mathrm{d}s \frac{J_0(s)}{\eta(r_s+\mathscr{B}sa)} \begin{pmatrix} 1 & 0 \\ 0 & 0 \end{pmatrix} + \frac{1}{(2\pi)} \begin{pmatrix} 1 & 0 \\ 0 & -1 \end{pmatrix} \int_0^\infty \mathrm{d}s \frac{1}{\eta(r_s+\mathscr{B}sa)} \frac{\mathrm{d}^2}{\mathrm{d}s^2} J_0(s)
\end{aligned} \tag{A 2}$$

† This statement is true for any bounded shape of the object, as the integration over the force profile in (2.12) does not alter the asymptotic behaviour of the flow far away from the object.

where in the last line we substituted $k = s/r_s$ under the integral. Two partial integrations of the second term in the last line in (A 2) lead to

$$
\begin{aligned}
2\pi \boldsymbol{O}(\boldsymbol{r}_s) &= \int_0^\infty \mathrm{d}s\, J_0(s) \begin{pmatrix} 1+\dfrac{\mathrm{d}^2}{\mathrm{d}s^2} & 0 \\ 0 & -\dfrac{\mathrm{d}^2}{\mathrm{d}s^2} \end{pmatrix} \frac{1}{\eta(r_s + \mathscr{B}sa)} \\
&\quad + \left[\begin{pmatrix} 1 & 0 \\ 0 & -1 \end{pmatrix} (-J_0(s)) \frac{\mathrm{d}}{\mathrm{d}s} \frac{1}{\eta(r_s + \mathscr{B}sa)} \right]_0^\infty \\
&= \begin{pmatrix} 1+(\mathscr{B}a)^2 \dfrac{\mathrm{d}^2}{\mathrm{d}r_s^2} & 0 \\ 0 & -(\mathscr{B}a)^2 \dfrac{\mathrm{d}^2}{\mathrm{d}r_s^2} \end{pmatrix} \frac{1}{(\eta \mathscr{B}a)} \int_0^\infty \mathrm{d}s\, J_0(s) \frac{1}{(r_s/\mathscr{B}a + s)} \\
&\quad - \frac{\mathscr{B}a}{\eta r_s^2} \begin{pmatrix} 1 & 0 \\ 0 & -1 \end{pmatrix}.
\end{aligned} \tag{A 3}
$$

In the last line in (A 3) we have replaced the differentiation with respect to s by a differentiation with respect to r_s. The remaining integral can be expressed by Struve and Bessel functions of the second kind (Gradshteyn & Ryshik 1981, 6.562-2)

$$
\begin{aligned}
\boldsymbol{O}(\boldsymbol{r}_s) &= \begin{pmatrix} 1+(\mathscr{B}a)^2 \dfrac{\mathrm{d}^2}{\mathrm{d}r_s^2} & 0 \\ 0 & -(\mathscr{B}a)^2 \dfrac{\mathrm{d}^2}{\mathrm{d}r_s^2} \end{pmatrix} \frac{1}{(2\pi\eta\mathscr{B}a)} \frac{\pi}{2} (\mathrm{H}_0(r_s/\mathscr{B}a) - N_0(r_s/\mathscr{B}a)) \\
&\quad - \frac{\mathscr{B}a}{(2\pi\eta r_s^2)} \begin{pmatrix} 1 & 0 \\ 0 & -1 \end{pmatrix} \\
&= \frac{1}{(4\eta r_s)} \left(\mathrm{H}_1(r_s/\mathscr{B}a) - N_1(r_s/\mathscr{B}a) - \frac{2\mathscr{B}a}{\pi r_s} \right) \begin{pmatrix} 1 & 0 \\ 0 & -1 \end{pmatrix} \\
&\quad + \frac{1}{(4\eta\mathscr{B}a)} (\mathrm{H}_0(r_s/\mathscr{B}a) - N_0(r_s/\mathscr{B}a)) \begin{pmatrix} 0 & 0 \\ 0 & 1 \end{pmatrix}.
\end{aligned} \tag{A 4}
$$

Noting that:

$$
\frac{\boldsymbol{r}_s \boldsymbol{r}_s}{r_s^2} = \begin{pmatrix} 1 & 0 \\ 0 & 0 \end{pmatrix} \quad \text{and} \quad \frac{\boldsymbol{\delta} r_s^2 - \boldsymbol{r}_s \boldsymbol{r}_s}{r_s^2} = \begin{pmatrix} 0 & 0 \\ 0 & 1 \end{pmatrix} \tag{A 5}
$$

we find (2.13*a*).

A.2. *Shallow water limit*

In the shallow water limit a similar treatment leads to

$$
\begin{aligned}
\boldsymbol{O}(\boldsymbol{r}_s) &= \frac{1}{(2\pi)} \int_0^\infty \mathrm{d}s \frac{s J_0(s)}{\eta\left(r_s^2/H + \mathscr{B}s^2 a\right)} \begin{pmatrix} 1 & 0 \\ 0 & 0 \end{pmatrix} \\
&\quad [4pt] + \frac{1}{(2\pi)} \begin{pmatrix} 1 & 0 \\ 0 & -1 \end{pmatrix} \int_0^\infty \mathrm{d}s \frac{s}{\eta\left(r_s^2/H + \mathscr{B}s^2 a\right)} \frac{\mathrm{d}^2}{\mathrm{d}s^2} J_0(s).
\end{aligned} \tag{A 6}
$$

The second integral in (A 6) can be expressed by the first by noting that

$$\begin{aligned}\int_0^\infty \mathrm{d}s \frac{s}{\alpha^2+s^2}\frac{\mathrm{d}^2}{\mathrm{d}s^2}J_0(s) &= -\int_0^\infty \mathrm{d}s \left(\frac{\mathrm{d}}{\mathrm{d}s}\frac{s}{\alpha^2+s^2}\right)\frac{\mathrm{d}}{\mathrm{d}s}J_0(s)\\ &= \frac{\mathrm{d}}{\mathrm{d}\alpha}\int_0^\infty \mathrm{d}s \left(\frac{\alpha}{\alpha^2+s^2}\right)\frac{\mathrm{d}}{\mathrm{d}s}J_0(s)\\ &= \frac{\mathrm{d}}{\mathrm{d}\alpha}\left.\frac{\alpha}{\alpha^2+s^2}J_0(s)\right|_0^\infty - \frac{\mathrm{d}}{\mathrm{d}\alpha}\int_0^\infty \mathrm{d}s\, J_0(s)\frac{\mathrm{d}}{\mathrm{d}s}\frac{\alpha}{\alpha^2+s^2}\\ &= -\frac{\mathrm{d}}{\mathrm{d}\alpha}\frac{1}{\alpha} - \frac{\mathrm{d}^2}{\mathrm{d}\alpha^2}\int_0^\infty \mathrm{d}s\,\frac{sJ_0(s)}{\alpha^2+s^2}. \end{aligned} \tag{A 7}$$

The first integral is (Gradshteyn & Ryshik 1981, 6.531-4)

$$\int_0^\infty \mathrm{d}s\,\frac{sJ_0(s)}{\alpha^2+s^2} = K_0(\alpha). \tag{A 8}$$

Insertion of (A 7) and (A 8) into (A 6) with $\alpha^2 = r_s^2/\mathscr{B}Ha$ yields the shallow water Oseen tensor in (2.23*b*).

Appendix B. Asymptotics

B.1. *Deep water limit, edge-on motion*

For $H \to \infty$ and small Boussinesq number and a constant force profile we find that

$$\begin{aligned}\bar{U} &= \frac{1}{2a}\int_{-a}^{a} u(x)\,\mathrm{d}x = \frac{F}{a^2}\int_0^{2a}\mathrm{d}(x-x')\,O_{xx}(|x-x'|\boldsymbol{e}_x)\int_0^{a-(x-x')/2}\mathrm{d}\frac{x+x'}{2}\\ &= \frac{F_{drag}}{4\pi\eta a}\int_0^{2/\mathscr{B}}\mathrm{d}s\left(\frac{2}{s}-\mathscr{B}\right)\left(\frac{\pi}{2}\mathrm{H}_1(s)-\frac{\pi}{2}N_1(s)-1/s\right)\\ &= \frac{F_{drag}}{4\pi\eta a}\left[-\mathscr{B}\left(s-\frac{\pi}{2}\mathrm{H}_0(s)+\frac{\pi}{2}N_0(s)-\ln(x)\right)\right]_0^{2/\mathscr{B}}\\ &\quad + \frac{F_{drag}}{4\pi\eta a}2\left[\operatorname{arcsinh}\left(\frac{1}{\mathscr{B}}\right)+\int_0^{2/\mathscr{B}}\frac{\mathrm{d}s}{s}\left(\frac{\pi}{2}\mathrm{H}_1(s)-\frac{\pi}{2}N_1(s)-1/s-\frac{s}{\sqrt{s^2+4}}\right)\right]\\ &= \frac{F_{drag}}{2\pi\eta a}\left[\ln\left(\frac{2}{\mathscr{B}}\right)+c-1+o(\mathscr{B})\right], \end{aligned} \tag{B 1}$$

where

$$c = \int_0^\infty \frac{\mathrm{d}s}{s}\left(\frac{\pi}{2}\mathrm{H}_1(s)-\frac{\pi}{2}N_1(s)-1/s-\frac{s}{\sqrt{s^2+4}}\right) \approx 0.276. \tag{B 2}$$

Combining (B 3) and (B 4) yields (3.6*a*).

B.2. *Shallow water limit, edge-on motion*

For $H \to 0$ we find by a similar treatment that:

$$\begin{aligned}\bar{U} &= \frac{FH}{2\pi\eta a^2}\frac{1}{\sqrt{\mathscr{B}H/a}}\int_0^{2/\sqrt{\mathscr{B}H/a}}\mathrm{d}s\left(\frac{1}{s}-K_1(s)\right)\left(\frac{1}{s}-\frac{\sqrt{\mathscr{B}H/a}}{2}\right)\\ &= \frac{FH}{2\pi\eta a^2}\frac{1}{\sqrt{\mathscr{B}H/a}}\int_0^{2/\sqrt{\mathscr{B}H/a}}\mathrm{d}s\,\frac{1}{s^2}\left(\ln\frac{s}{2}+\gamma+K_0(s)\right)\end{aligned}$$

$$\approx \frac{FH}{2\pi\eta a^2}\frac{1}{\sqrt{\mathscr{B}H/a}}\left[c' - \int_{2/\sqrt{\mathscr{B}H/a}}^{\infty} \mathrm{d}s\,\frac{1}{s^2}\left(\ln\frac{s}{2}+\gamma\right)\right] + o(\mathscr{B}^{3/2})$$

$$\approx \frac{FH}{4\eta a^2}\frac{1}{\sqrt{\mathscr{B}H/a}}\left(1+\frac{\sqrt{\mathscr{B}H/a}}{\pi}\left(\ln\frac{1}{\sqrt{\mathscr{B}H/a}}+\gamma+1\right)\right), \tag{B 3}$$

where

$$c' = \int_0^{\infty} \mathrm{d}s\,\frac{1}{s^2}\left(\ln\frac{s}{2}+\gamma+K_0(s)\right) \approx \pi/2. \tag{B 4}$$

Equation (B 3) is equivalent to (3.6*b*). The derivation of the asymptotic behaviour for broadside-on motion of the needle follows similar lines.

Appendix C. Numerics

We approximate the force profile $\tau_x(x)$ by

$$\tau_x(x) = \tau_i \quad \text{for} \quad x_i - h/2 < x < x_i + h/2, \tag{C 1}$$

where the x_i are points spaced at a distance $h < \mathscr{B}a$ or $h < \sqrt{\mathscr{B}Ha}$ on the needle. The velocity u_i at position x_i is then given by

$$u_i = A_{ij}\tau_j, \tag{C 2}$$

where A_{ij} is a Toeplitz matrix given by

$$A_{ij} = \int_{x_j-x_i-h/2}^{x_j-x_i+h/2} O_{xx}(x\boldsymbol{e}_x)\,\mathrm{d}x \approx \begin{cases} \dfrac{h}{4\pi\eta\mathscr{B}a}\left(\ln\dfrac{4\mathscr{B}a}{h}-\gamma+3/2\right) & \text{for } i=j,\ H\to\infty \\ \dfrac{h}{4\pi\eta\mathscr{B}a}\left(\ln\dfrac{4\sqrt{\mathscr{B}Ha}}{h}-\gamma+3/2\right) & \text{for } i=j,\ H\to 0 \\ h\times O_{xx}((x_i-x_j)\boldsymbol{e}_x) & \text{for } i\neq j \end{cases} \tag{C 3}$$

for the edge-on motion and

$$A_{ij} = \int_{y_j-y_i-h/2}^{y_j-y_i+h/2} O_{xx}(y\boldsymbol{e}_y)\,\mathrm{d}y \approx \begin{cases} \dfrac{h}{4\pi\eta\mathscr{B}a}\left(\ln\dfrac{4\mathscr{B}a}{h}-\gamma+1/2\right) & \text{for } i=j,\ H\to\infty \\ \dfrac{h}{4\pi\eta\mathscr{B}a}\left(\ln\dfrac{4\sqrt{\mathscr{B}Ha}}{h}-\gamma+1/2\right) & \text{for } i=j,\ H\to 0 \\ h\times O_{xx}((y_i-y_j)\boldsymbol{e}_x) & \text{for } i\neq j \end{cases} \tag{C 4}$$

for the broadside-on motion. The force profile is found by the inversion of (C 2) using Trench's (Trench 1964) algorithm.

$$\tau_i = (A^{-1})_{ij}u_j \tag{C 5}$$

where $u_j = U$ for all j. The drag force is then given by

$$F_{drag} = h\times\sum_i \tau_i. \tag{C 6}$$

REFERENCES

Barentin, C., Ybert, C., DiMeglio, J. M. & Joanny, J. F. 1999 Surface shear viscosity of Gibbs and Langmuir monolayers. *J. Fluid Mech.* **397**, 331–349.

Brooks, C. F., Fuller, G. G., Frank, C. W. & Robertson, C. R. 1999 An interfacial stress rheometer to study rheological transitions in monolayers at the air-water interface. *Langmuir* **15**, 2450–2459.

Ding, J. Q., Warriner, H. E., Zasadzinski, J. A. & Schwartz, D. K. 2002 Magnetic needle viscometer for Langmuir monolayers. *Langmuir* **18**, 2800–2806.

Ding, J. Q., Warriner, H. E. & Zasadzinski, J. A. 2002 Viscosity of two-dimensional suspensions. *Phys. Rev. Lett.* **88**, 168102.

Fourt, L. & Harkins, W. D. 1938 Surface Viscosity of long-chain alcohol monolayers. *J. Phys. Chem.* **42**, 897–910.

Ghaskadvi, R. S., Ketterson, J. B., MacDonald, R. C. & Dutta, P. 1997 Apparatus to measure the shear modulus of Langmuir monolayers as functions of strain amplitude and frequency. *Rev. Sci. Instrum.* **68**, 1792–1795.

Goodrich, F. C. & Chatterjee, A. K. 1970 Theory of absolute surface shear viscosity 2. Rotating disk problem. *J. Colloid Interface Sci.* **34**, 36.

Goodrich, F. C., Allen, L. H. & Poskanzer, A. 1975 New surface viscometer of high sensitivity 1. Theory. *J. Colloid Interface Sci.* **52**, 201–212.

Gradshteyn, I. S. & Ryzhik, I. M. 1981 *Tables of Series, Products, and Integrals.* Harri Deutsch, Thun, Frankfurt/M.

Happel, J. & Brenner, H. 1983 *Low Reynolds Number Hydrodynamics.* Martinus Nijhoff.

Harkins, W. D. & Myers, R. J. 1937 Viscosity of monomolecular films. *Nature* **140**, 465.

Hughes, B. D., Pailthorpe, B. A. & White, L. R. 1981 The translational and rotational drag on a cylinder moving in a membrane. *J. Fluid Mech.* **110**, 349–372.

Jarvis, N. L. 1965 Surface viscosity of monomolecular films of long-chain aliphatic amides, amines, alcohols, and carboxylic acids. *J. Phys. Chem.* **69**, 1789–1797.

Klingler, J. F. & McConnell, H. 1993 Brownian-motion and fluid-mechanis of lipid monolayer domains. *J. Phys. Chem.* **97**, 6096–6100.

Langmuir, I. & Schaefer, V. J. 1937 The effect of dissolved salts on insoluble monolayers. *J. Am. Chem. Soc.* **59**, 2400–2414.

Levine, A. J., Liverpool, T. B. & MacKintosh, F. C. 2003 On the mobility of extended bodies in viscous films and membranes. Preprint (Los Alamos server, cond-mat 0303095).

Lifshutz, N., Hegde, M. G. & Slattery, J. C. 1971 knife-edge surface viscometers. *J. Colloid Interface Sci.* **37**, 73–79.

Mannheimer, R. J. & Schechter, R. S. 1970 An improved apparatus and analysis fro surface rheological measurements. *J. Colloid Interface Sci.* **32**, 195–211.

Oh, S. G. & Slattery, J. C. 1978 Disk and binocal interfacial viscometers. *J. Colloid Interface Sci.* **67**, 516–525.

Saffman, P. G. & Delbrück, M. 1975 Brownian-motion in biological-membranes. *Proc. Natl Acad. Sci. USA* **72**, 3111–3113.

Schwartz, D., Knobler, C. M. & Bruinsma, R. 1994 Direct observation of Langmuir monolayer flow-through a channel. *Phys. Rev. Lett.* **73**, 2841–2844.

Shahin, G. T. Jr 1986 The stress deformation interfacial rheometer. Dissertation, University of Pennsylvania.

Steffen, P., Heinig, P., Wurlitzer, S., Khattari, Z. & Fischer Th. M. 2001 The translational and rotational drag on Langmuir monolayer domains. *J. Chem. Phys.* **115**, 994–997.

Stone, H. A. & Ajdari, A. 1998 Hydrodynamics of particles embedded in a flat surfactant layer overlying a subphase of finite depth. *J. Fluid Mech.* **369**, 151–173.

Trench, W. F. 1964 An algorithm for the inversion of finite Toeplitz matrices. *J. Soc. Indust. Appl. Maths* **12**, 515–522.

Wurlitzer, S., Schmiedel, H. & Fischer, Th. M. 2002 Electrophoretic relaxation dynamics of domains in Langmuir monolayers. *Langmuir* **18**, 4393–4400.